Scilight

Nonlinear Analysis and Computer Simulations
https://www.sciltp.com/journals/nacs

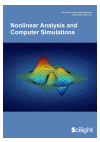

Article

On the Evolution of Internal Variables for Anisotropic Viscoelastic Media

Armando Ciancio [1], Bruno Felice Filippo Flora [2] and Vincenzo Ciancio [3,*]

[1] Department of Biomedical and Dental Sciences and Morphofunctional Imaging, University of Messina, A.O.U. Policlinico "G. Martino", Via Consolare Valeria, 98125 Messina, Italy
[2] Azienda Ospedaliera "Papardo", V.le Ferdinando Stagno D'Alcontres, 98158 Messina, Italy
[3] Accademia Peloritana dei Pericolanti, University of Messina, Piazza S. Pugliatti 1, 98121 Messina, Italy
* Correspondence: vincenzo.ciancio@accademiapeloritana.it

How To Cite: Ciancio, A.; Flora, B.F.F.; Ciancio, V. On the Evolution of Internal Variables for Anisotropic Viscoelastic Media. *Nonlinear Analysis and Computer Simulations* **2026**, *1*(3), 12. https://doi.org/10.53941/nacs.2026.100012

Received: 2 May 2026
Revised: 3 June 2026
Accepted: 25 June 2026
Published: 14 July 2026

Abstract: The description of viscoelastic media with memory requires a thermodynamic formalism capable of capturing irreversible processes. In this work, a physical-mathematical model for anisotropic viscoelastic materials is developed based on the V. Ciancio—G.A. Kluitenberg theory. The generalized evolution equation is derived, showing its connection with modified Euler-Lagrange equations and the Rayleigh dissipation function. A direct and explicit reduction to the classical Maxwell model for viscoelasticity is demonstrated in the appropriate limit, confirming the consistency of the proposed framework. This work aims to offer a unified theoretical framework, providing a solid foundation for future developments.

Keywords: thermodynamics of continuum; rheology; materials of stress-rate and internal-variable type; anisotropic; heat flow

2020 MSC: 80A17; 76Axx; 74Axx; 74E10; 80A20

1. Introduction

The study of viscoelastic media plays a central role in many branches of continuum physics. A particularly fruitful way to address this complexity is the introduction of internal variables ξ_α, dating back to Meixner [1], G.A. Kluitenberg and V. Ciancio [2–11]. This approach enriches the space of thermodynamic states to describe microscopic processes without explicitly modeling their complete dynamics.

1.1. The V. Ciancio—G.A. Kluitenberg Theory

In the context of the V. Ciancio—G.A. Kluitenberg theory, internal variables ξ_α are associated with relaxation and dissipation processes [12–14]. The distinguishing feature of this approach is the careful attention to the algebraic structure of constitutive tensors and the systematic use of non-equilibrium thermodynamics to ensure consistency with the second law. This framework has been successfully applied to describe a wide range of phenomena, including viscoelasticity, dielectric relaxation, and thermal diffusion. A key aspect of the present work is the interpretation of internal variables as configurational degrees of freedom endowed with their own inertia. As proved in Theorem 1, the modified Euler-Lagrange equations provide a variational framework for dissipative systems and in Theorem 2, this leads to second-order evolution equations of the type:

$$I_{\alpha\beta}\ddot{\xi}_\beta + \gamma_{\alpha\beta}\dot{\xi}_\beta + K_{\alpha\beta}\xi_\beta = -\gamma_{\alpha\mu}L_{\mu\beta}\frac{A_\beta}{T} - \gamma_{\alpha\mu}\mathbf{L}_{\mu 0}\cdot\frac{\nabla T}{T^2}, \tag{1}$$

where $I_{\alpha\beta}$ represents configurational inertia, $\gamma_{\alpha\beta}$ is the dissipation tensor, $K_{\alpha\beta}$ is the elastic recall tensor, $L_{\alpha\beta}$ are Onsager mobility coefficients, and $\mathbf{L}_{\mu 0}$ couples thermal gradients to internal variable evolution.

1.2. Original Contributions

This manuscript provides the following novel contributions:

- Second-order Dynamics: A rigorous derivation of a generalized, second-order evolution equation for internal variables, extending classical first-order Onsagerian kinetics.
- Variational Structure: The explicit connection between the Rayleigh dissipation function and the coupling coefficients in the evolution equation, providing a Lagrangian framework for dissipative systems.
- Hybrid Heat Conduction: The incorporation of a hybrid (Fourier-Cattaneo) heat conduction law, leading to a generalized heat equation that bridges diffusive and wave-like thermal transport.
- Bridge to Classical Models: A direct and explicit demonstration of how the proposed model reduces to the classical Maxwell model for viscoelasticity in the appropriate limit.

1.3. Comparison with the Classical Maxwell Model

To appreciate the generality of the proposed framework, it is instructive to compare it with the classical Maxwell model of viscoelasticity [15]. The Maxwell model, proposed by James Clerk Maxwell in 1867, represents the simplest description of a viscoelastic fluid and is governed by the differential equation:

$$\dot{\varepsilon} = \frac{\dot{\tau}}{E} + \frac{\tau}{\eta}, \tag{2}$$

where ε is the strain, τ the stress, E the elastic modulus, and η the viscosity. This model predicts exponential stress relaxation with characteristic time $\tau_M = \eta/E$ and captures the essential physics of materials that exhibit both instantaneous elasticity and viscous flow. The Maxwell model can be interpreted within an internal variable framework. Introducing an internal variable ξ representing the inelastic (viscous) strain, the total strain is decomposed as $\varepsilon = \varepsilon_{el} + \varepsilon_{vis}$, with $\tau = E\varepsilon_{el}$ and $\dot{\varepsilon}_{vis} = \tau/\eta$. This leads to the evolution equation $\dot{\xi} = -\frac{1}{\tau_M}\xi +$ (strain rate term), which is a first-order kinetic equation. The present work extends this classical picture in several fundamental directions:

1. Second-order dynamics: Unlike the Maxwell model, which assumes instantaneous relaxation (first-order kinetics), Equation (1) includes an inertial term $I_{\alpha\beta}\ddot{\xi}_\beta$. This allows the description of phenomena where internal variables exhibit wave-like behavior or finite propagation speed, a feature absent in classical rate-dependent theories.
2. Thermal coupling: The terms involving $\nabla T/T^2$ couple mechanical relaxation with thermal transport, enabling the modeling of thermomechanical effects such as thermal stress relaxation and heat-induced internal rearrangements.
3. Anisotropy: The tensorial nature of all coefficients ($I_{\alpha\beta}$, $\gamma_{\alpha\beta}$, $K_{\alpha\beta}$, $L_{\alpha\beta}$) allows the description of fully anisotropic materials, a capability not present in the isotropic Maxwell model.
4. Multiple relaxation mechanisms: The index α can span multiple internal variables, each with its own characteristic relaxation time, allowing the representation of complex relaxation spectra (e.g., Wiechert or Prony series models).

Importantly, the classical Maxwell model is recovered from (1) in the following limiting cases:

- Isothermal conditions ($\nabla T = 0$),
- Overdamped regime ($I_{\alpha\beta} \to 0$, $K_{\alpha\beta} \to 0$),
- Single internal variable ($\alpha = 1$),
- Isotropic materials (scalar coefficients),
- Specific elasticity constraint $D^2 = C^{(0)}B$ (as shown in Section 6).

Thus, the proposed framework provides a rigorous generalization of the Maxwell model, incorporating inertia, thermal effects, anisotropy, and multiple relaxation channels within a thermodynamically consistent Lagrangian formalism.

The remainder of this paper is organized as follows. Section 2 reviews recent developments in internal variable theories for viscoelasticity (2015–2025). Section 3 presents the modified Euler-Lagrange equations with Rayleigh dissipation, establishing the variational foundation of the model. Section 4 rigorously derives the connection between Onsager's phenomenological relations and the generalized evolution equation. Section 5 provides an explicit comparison with the Maxwell model, demonstrating the recovery of classical results. Section 6 presents numerical simulations of the hybrid heat equation and compares it with the Maxwell-Cattaneo (telegraph) model. Finally, Section 7 concludes the paper with a summary and outlook. The complete list of symbols can be found in Appendix A.

2. Recent Developments in Viscoelasticity with Internal Variables (2015–2025)

In recent years, the modeling of viscoelastic media with internal variables has undergone significant developments, driven by the need to capture complex behaviors such as memory effects, nonlinear dissipation, and multiscale coupling phenomena.

2.1. Thermodynamic Frameworks and Internal Variables

A central trend has been the reinforcement of thermodynamic consistency. Berezovski and Ván (2015) investigated the thermodynamic origin of microinertia within internal variable theories [16]. Ref. [17] incorporated internal variables into viscoelastic and thermoelastic formulations. Ref. [18] developed a rigorous thermodynamic framework for viscoelastic fluids with heat conduction, proving the existence of global weak solutions.

2.2. Nonlinear and Multiscale Modeling Approaches

Ref. [19] introduced a reactive inelasticity framework based on internal variables for biological tissues. Ref. [20] proposed a thermodynamically consistent viscoelastic model accounting for microstructural evolution in polymers. Ref. [21] demonstrated that quasi-linear viscoelastic (QLV) models can be reformulated using internal variables.

2.3. Fractional and Generalized Viscoelastic Models

Fractional viscoelastic models provide a powerful framework for describing memory effects over multiple time scales. Recent works have introduced fractional derivatives into internal variable formulations, leading to generalized constitutive equations capable of reproducing complex relaxation spectra [22] and for viscoanelastic model [23].

2.4. Discussion and Positioning

The reviewed literature highlights a key limitation: most models either remain first-order in internal variables or neglect configurational inertia. The present work addresses this gap by introducing second-order evolution equations and explicitly capturing the transition between diffusive and wave-like regimes.

3. Modified Euler-Lagrange Equations with Rayleigh Dissipation

A crucial aspect of the theory is the connection between the phenomenological equations and the generalized evolution equation, which has the structure of a Newtonian equation of motion for internal variables. Analogously to the Rayleigh dissipation function [24] to describe mechanical systems with dissipative forces proportional to velocity, i.e., it is a thermodynamic potential that describes the energy dissipated by viscous friction. Its formal definition is:

Definition 1 (Rayleigh Dissipation Function)**.** *For a system with dissipative forces proportional to velocities, the Rayleigh dissipation function $\mathcal{R}$ is defined as:*

$$\mathcal{R} = \frac{1}{2}\gamma_{\alpha\beta}\dot{\xi}_\alpha\dot{\xi}_\beta \tag{3}$$

where $\dot{\xi}_\alpha = d\xi_\alpha/dt$, and $\gamma_{\alpha\beta}$ is the dissipation tensor, symmetric and positive definite. The Einstein summation convention applies to repeated indices.

Theorem 1 (Modified Euler-Lagrange Equations with Dissipation)**.** *For a mechanical system described by the Lagrangian $\mathcal{L}(\xi_\alpha, \dot{\xi}_\alpha, t)$ and the Rayleigh dissipation function $\mathcal{R}(\dot{\xi}_\alpha)$, the equations of motion are:*

$$\frac{d}{dt}\left(\frac{\partial\mathcal{L}}{\partial\dot{\xi}_\alpha}\right) - \frac{\partial\mathcal{L}}{\partial\xi_\alpha} + \frac{\partial\mathcal{R}}{\partial\dot{\xi}_\alpha} = Q_\alpha \tag{4}$$

where Q_α are the generalized non-conservative forces not derivable from potentials.

Proof. The proof proceeds by extending Hamilton's principle. For a conservative system, Hamilton's principle yields the Euler-Lagrange equations. For non-conservative forces, d'Alembert's principle provides the fundamental variational statement. The virtual work done by applied forces is $\delta W = Q_\alpha^{(nc)}\delta\xi_\alpha$. For viscous damping forces, $Q_\alpha^{(diss)} = -\partial\mathcal{R}/\partial\dot{\xi}_\alpha$. Substituting and requiring the variation to vanish for arbitrary independent $\delta\xi_\alpha$ yields (4). □

Example 1 (Application to Internal Variables)**.** *For internal variables ξ_α (dimensionless) with a Lagrangian that includes configurational kinetic energy and potential energy:*

$$\mathcal{L}(\xi_\alpha, \dot{\xi}_\alpha) = \frac{1}{2} I_{\alpha\beta} \dot{\xi}_\alpha \dot{\xi}_\beta - \frac{1}{2} K_{\alpha\beta} \xi_\alpha \xi_\beta - \Pi_{int}(\xi_\alpha), \tag{5}$$

and Rayleigh dissipation function $\mathcal{R} = \frac{1}{2}\gamma_{\alpha\beta}\dot{\xi}_\alpha\dot{\xi}_\beta$, the modified Euler-Lagrange equations give:

$$I_{\alpha\beta}\ddot{\xi}_\beta + \gamma_{\alpha\beta}\dot{\xi}_\beta + K_{\alpha\beta}\xi_\beta + \frac{\partial \Pi_{int}}{\partial \xi_\alpha} = Q_\alpha^{(ext)}. \tag{6}$$

In thermodynamic systems, $\partial\Pi_{int}/\partial\xi_\alpha = A_\alpha$ are the conjugate thermodynamic forces, and $Q_\alpha^{(ext)}$ includes thermal coupling terms.

4. Connection between Phenomenological and Evolution Equations

Theorem 2 (Connection between Phenomenological and Evolution Equations)**.** *Let the internal variables ξ_α (dimensionless) be governed by the Onsager phenomenological relations (see [12]):*

$$\dot{\xi}_\alpha = -L_{\alpha\beta}\frac{A_\beta}{T} - \mathbf{L}_{\alpha 0} \cdot \frac{\nabla T}{T^2}, \tag{7}$$

where A_β are the conjugate thermodynamic forces with dimensions of pressure (Pa), T is the absolute temperature (K), $L_{\alpha\beta}$ is the mobility matrix (symmetric, positive definite), and $\mathbf{L}_{\alpha 0}$ is the thermal coupling vector. The Onsager relation (7) expresses the flux $\dot{\xi}_\alpha$ as a linear combination of the thermodynamic forces A_β/T and $\nabla T/T^2$, where summation over the repeated index β is implied (Einstein summation convention). The index α is instead a free index, and the equation holds for each α. The coefficients $L_{\alpha\beta}$ and $\mathbf{L}_{\alpha 0}$ are the Onsager coefficients, which satisfy the well-known reciprocity relations. Consider the generalized evolution equation obtained from the Lagrangian formulation with Rayleigh dissipation:

$$I_{\alpha\beta}\ddot{\xi}_\beta + \gamma_{\alpha\beta}\dot{\xi}_\beta + K_{\alpha\beta}\xi_\beta = -L^{(e)}_{\alpha\beta}\frac{A_\beta}{T} - \mathbf{L}^{(e)}_{\alpha 0} \cdot \frac{\nabla T}{T^2}, \tag{8}$$

where $I_{\alpha\beta}$ is the configurational inertia tensor, $\gamma_{\alpha\beta}$ the dissipation tensor, $K_{\alpha\beta}$ the elastic recall tensor, and $L^{(e)}_{\alpha\beta}$, $\mathbf{L}^{(e)}_{\alpha 0}$ are the coupling coefficients in the evolution equation. For the two equations to be consistent in the overdamped limit ($I_{\alpha\beta} \to 0$, $K_{\alpha\beta} \to 0$), the following relations must hold:

$$L^{(e)}_{\alpha\beta} = \gamma_{\alpha\mu} L_{\mu\beta}, \qquad \mathbf{L}^{(e)}_{\alpha 0} = \gamma_{\alpha\mu}\mathbf{L}_{\mu 0}. \tag{9}$$

Therefore, the coupling coefficients in the evolution equation are obtained by multiplying the phenomenological coefficients by the dissipation tensor $\gamma_{\alpha\beta}$.

Proof. The proof proceeds in five steps: dimensional analysis, the overdamped limit, the consistency condition, dimensional verification, and the final form. In the overdamped limit ($I_{\alpha\beta} \to 0, K_{\alpha\beta} \to 0$), Equation (8) reduces to $\gamma_{\alpha\beta}\dot{\xi}_\beta = -L^{(e)}_{\alpha\beta}A_\beta/T - \mathbf{L}^{(e)}_{\alpha 0} \cdot \nabla T/T^2$. Multiplying the Onsager relation (7) by $\gamma_{\alpha\beta}$ gives $\gamma_{\alpha\beta}\dot{\xi}_\beta = -\gamma_{\alpha\mu}L_{\mu\beta}A_\beta/T - \gamma_{\alpha\mu}\mathbf{L}_{\mu 0} \cdot \nabla T/T^2$. For consistency, the coefficients of the independent thermodynamic forces must be equal, yielding (9). □

Corollary 1 (Overdamped limit recovery)**.** *In the overdamped limit ($I_{\alpha\beta} \to 0$, $K_{\alpha\beta} \to 0$), Equation (8) reduces to Onsager's original relation (7), demonstrating that the generalized evolution equation is a consistent extension of classical irreversible thermodynamics.*

Remark 1 (Physical interpretation of the coupling relations)**.** *The relations $L^{(e)}_{\alpha\beta} = \gamma_{\alpha\mu}L_{\mu\beta}$ reveal that the dissipation tensor $\gamma_{\alpha\beta}$ acts as a "metric" that connects the phenomenological mobility coefficients $L_{\alpha\beta}$ to the coupling coefficients $L^{(e)}_{\alpha\beta}$, establishing a direct link between variational principles and thermodynamic constraints.*

5. Hybrid Heat Equation, Limiting Regimes, and Dispersion Analysis

Within the internal-variable framework, the total heat flux is decomposed into a diffusive (Fourier) part and a relaxing (Cattaneo-type) part [12] :

$$\mathbf{q} = \mathbf{q}^{(0)} + \mathbf{q}^{(1)}, \qquad \mathbf{q}^{(0)} = -k\nabla T, \tag{10}$$

$$\tau_q \, \dot{\mathbf{q}}^{(1)} + \mathbf{q}^{(1)} = -k_1 \nabla T, \tag{11}$$

where k and k_1 are thermal conductivities, and $\tau_q > 0$ is a relaxation time associated with heat flux. Equation (11) is the Maxwell–Cattaneo–Vernotte (MCV) law [25–27]. The energy balance (in absence of sources) reads:

$$\rho c \dot{T} + \nabla \cdot \mathbf{q} = 0, \tag{12}$$

with ρ density and c specific heat. Combining (10)–(12) yields a hybrid heat equation. Eliminating $\mathbf{q}^{(1)}$ by taking the divergence of (11) and using (12), one obtains:

$$\rho c \dot{T} - k\nabla^2 T + \tau_q \, \rho c \ddot{T} - \tau_q k \, \nabla^2 \dot{T} = k_1 \nabla^2 T. \tag{13}$$

Rearranging terms:

$$\tau_q \rho c \ddot{T} + \rho c \dot{T} - (k + k_1)\nabla^2 T - \tau_q k \, \nabla^2 \dot{T} = 0. \tag{14}$$

Equation (14) is a generalized heat equation that interpolates between diffusive (Fourier) and wave-like (Cattaneo) regimes, under the assumption that:

$$\frac{d}{dt} = \partial_t + \mathbf{v} \cdot \nabla = \partial_t$$

with $\mathbf{v} = 0$, consider the following cases:

5.1. Limiting Cases: Fourier vs. Cattaneo Regimes

5.1.1. Fourier Limit ($\tau_q \to 0$)

When relaxation effects are negligible, $\tau_q \to 0$, Equation (14) reduces to the classical Fourier heat equation:

$$\rho c \dot{T} = (k + k_1)\nabla^2 T. \tag{15}$$

This regime exhibits infinite propagation speed and purely diffusive behavior.

5.1.2. Cattaneo (Hyperbolic) Limit

If the Fourier part is negligible ($k \approx 0$) and relaxation dominates, Equation (14) reduces to a damped wave equation:

$$\tau_q \rho c \ddot{T} + \rho c \dot{T} - k_1 \nabla^2 T = 0, \tag{16}$$

which is the telegraph equation. The associated thermal wave speed is:

$$c_{\text{th}} = \sqrt{\frac{k_1}{\rho c \, \tau_q}}, \tag{17}$$

indicating finite-speed propagation.

5.2. Dispersion Relation and Attenuation

Consider the hybrid heat equation (see [12]):

$$\tau_q \rho c \frac{\partial^2 T}{\partial t^2} + \rho c \frac{\partial T}{\partial t} = (k + k_1)\nabla^2 T + k\tau_q \nabla^2 \frac{\partial T}{\partial t}, \tag{18}$$

where $T(\mathbf{x}, t)$ is the temperature, ρ the density, c the specific heat, k and k_1 thermal conductivities, τ_q the heat flux relaxation time.

5.2.1. Plane Waves and Dispersion Relation

We seek plane wave solutions of the form:

$$T(\mathbf{x}, t) = \hat{T}\, e^{i(\mathbf{k}\cdot\mathbf{x}-\omega t)}, \tag{19}$$

with $\mathbf{k}$ the wave vector ($k = |\mathbf{k}|$) and ω the complex frequency. Substituting into (18):

$$\begin{aligned} &\tau_q \rho c(-\omega^2) + \rho c(-i\omega) \\ &\quad = (k + k_1)(-k^2) + k\tau_q(-k^2)(-i\omega). \end{aligned} \tag{20}$$

Rearranging terms yields the dispersion relation:

$$-\tau_q \rho c\, \omega^2 - i\rho c\, \omega + (k + k_1)k^2 + i\tau_q k\, \omega k^2 = 0. \tag{21}$$

5.2.2. Hyperbolic Regime ($k \approx 0$)

In the small wavenumber limit, we seek an approximate solution of the form:

$$\omega = \pm c_{\text{th}} k - i\gamma, \tag{22}$$

with γ a positive real number (attenuation rate) and c_{th} to be determined. Substituting into (21) and neglecting higher-order terms (k^3, k^4):

- The term $-\tau_q \rho c \omega^2$ contributes $-\tau_q \rho c(c_{\text{th}}^2 k^2 \mp 2ic_{\text{th}} k\gamma - \gamma^2)$
- The term $-i\rho c\omega$ contributes $-i\rho c(\pm c_{\text{th}} k - i\gamma) = \mp i\rho c c_{\text{th}} k - \rho c\gamma$
- The term $(k + k_1)k^2$ remains unchanged
- The term $i\tau_q k\omega k^2 \sim O(k^3)$ is negligible

Imposing $c_{\text{th}}^2 = (k+k_1)/(\tau_q \rho c)$ (non-dissipative propagation condition), the terms $-\tau_q \rho c c_{\text{th}}^2 k^2$ and $(k+k_1)k^2$ cancel. Collecting terms in k and constant terms:

$$\text{Terms in } k: \quad 2i\tau_q \rho c c_{\text{th}} \gamma k \mp i\rho c c_{\text{th}} k = i\rho c c_{\text{th}}(2\tau_q \gamma \mp 1)k = 0, \tag{23}$$

$$\text{Constant terms:} \quad \tau_q \rho c \gamma^2 - \rho c \gamma = \rho c \gamma(\tau_q \gamma - 1) = 0. \tag{24}$$

The physically relevant solution is $\gamma = 1/(2\tau_q)$, which satisfies both equations. We thus obtain:

$$\boxed{\omega \approx \pm c_{\text{th}} k - i\frac{1}{2\tau_q}}, \qquad c_{\text{th}} = \sqrt{\frac{k + k_1}{\tau_q \rho c}}. \tag{25}$$

5.2.3. Physical Interpretation

- Wave-like propagation: The real part $\pm c_{\text{th}} k$ describes thermal waves propagating with finite speed c_{th}, overcoming the paradox of classical diffusion (infinite speed) [25].
- Exponential attenuation: The imaginary part $-1/(2\tau_q)$ causes a temporal decay $e^{-t/(2\tau_q)}$, independent of the wavenumber at this order of approximation.
- Relaxation time: τ_q represents the delay time in the heat flux response to the temperature gradient. In the limit $\tau_q \to 0$, classical diffusive behavior is recovered:

$$\omega \approx -i\frac{k + k_1}{\rho c} k^2, \tag{26}$$

  which describes purely diffusive decay without wave propagation.
- Diffusion-wave transition: At low frequencies (small k), diffusive behavior dominates, while at high frequencies (large k), the hyperbolic nature with wave propagation emerges.

5.3. Numerical Method

The numerical simulation of the coupled thermomechanical system is performed using a high-resolution finite difference method. The algorithm is summarized below:

Listing 1: Algorithm for hybrid heat equation with internal variables

```
ALGORITHM: Hybrid Heat Equation with Internal Variables (Overdamped Regime)

INPUT:
Domain: x in [-L/2, L/2] with L = 4.0 m
Spatial discretization: nx = 100 points, dx = L/nx
Time parameters: t_end = 6.0 s, dt = 0.002 s
Thermal parameters: alpha = 0.005, beta = 0.60, tau_q = 0.8 s
Internal variables: n_xi = 2, I = [0.6, 0.8], gamma = [0.12, 0.15], K =
    [0.5, 0.6]
Initial condition: T(x,0) = Gaussian + Ricker wavelet + secondary pulses

METHOD:
1. Initialize fields: T(x,0), s(x,0), xi(x,0), xi_dot(x,0)
2. For each time step n = 0 to nt:
Compute spatial derivatives via centered finite differences
Compute thermodynamic forces: A = B*xi + D*epsilon
Compute dissipation: Q_diss = A * xi_dot / (rho * c * T)
Compute RHS: dT/dt, ds/dt, xi_ddot via evolution equations
Update fields with 4th-order Runge-Kutta
Enforce boundary conditions
3. Save snapshots every dt_save = 0.05 s
4. Generate visualizations

OUTPUT:
- Temperature evolution T(x,t) for x in [-2,2] m, t in [0,6] s
- Internal variable evolution xi_1(x,t), xi_2(x,t)
- Peak temperature decay curve
- Oscillation frequency and damping rate
```

The numerical scheme employs a fourth-order Runge-Kutta integrator for temporal discretization, ensuring second-order accuracy in space and fourth-order accuracy in time. The stability condition requires $\Delta t < \min(\Delta x^2/(2\alpha), 2\tau_q)$, which is satisfied with $\Delta t = 0.002$ s.

5.4. Simulation Results

The following figures present the results of the numerical simulation, which captures the overdamped oscillatory behavior of the temperature field resulting from the coupling between thermal diffusion, hyperbolic heat waves (Maxwell-Cattaneo), and internal variable dynamics.

5.4.1. Initial Temperature Profile

The initial temperature distribution $\Delta T(x)$ is modeled as a superposition of a central Gaussian peak and two symmetric secondary lobes, representing localized thermal perturbations Figure 1. The analytical expression is given by:

$$\Delta T(x) = Z_1 \cdot e^{-\frac{x^2}{2m_1^2}} + Z_2 \cdot \left[e^{-\frac{(x-0.5)^2}{2m_2^2}} + e^{-\frac{(x+0.5)^2}{2m_2^2}} \right] \tag{27}$$

where:

- x is the spatial coordinate (in meters);
- $Z_1 = 40.7$ is the amplitude of the central Gaussian peak;
- $m_1 = 0.18$ m is the standard deviation of the central peak, which controls its width (smaller values yield a narrower, sharper peak);
- $Z_2 = 5.2$ is the amplitude of the secondary lobes;
- $m_2 = 0.15$ m is the standard deviation of the lateral Gaussians, determining the smoothness and spread of the lobes centered at $x = \pm 0.5$ m.

This functional form captures a main thermal anomaly at $x = 0$ with sharp localization, flanked by two smaller, broader perturbations symmetrically placed at ± 0.5 m. The ratio $Z_2/Z_1 \approx 0.128$ indicates that the secondary lobes

contribute approximately 12.8% of the central peak amplitude, making them significant but subordinate features of the temperature field. Figure 2 shows the complete temperature profile along with its individual components.

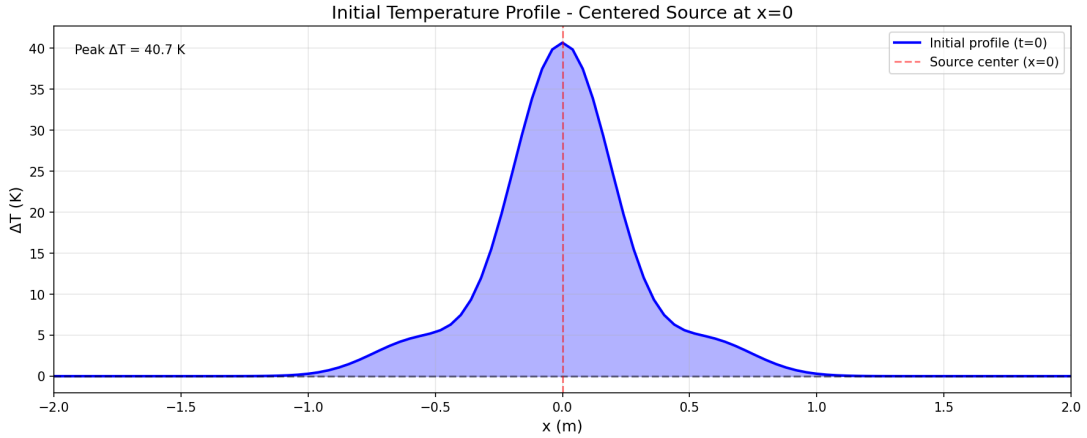

Figure 1. Initial temperature profile at $t = 0$ s.

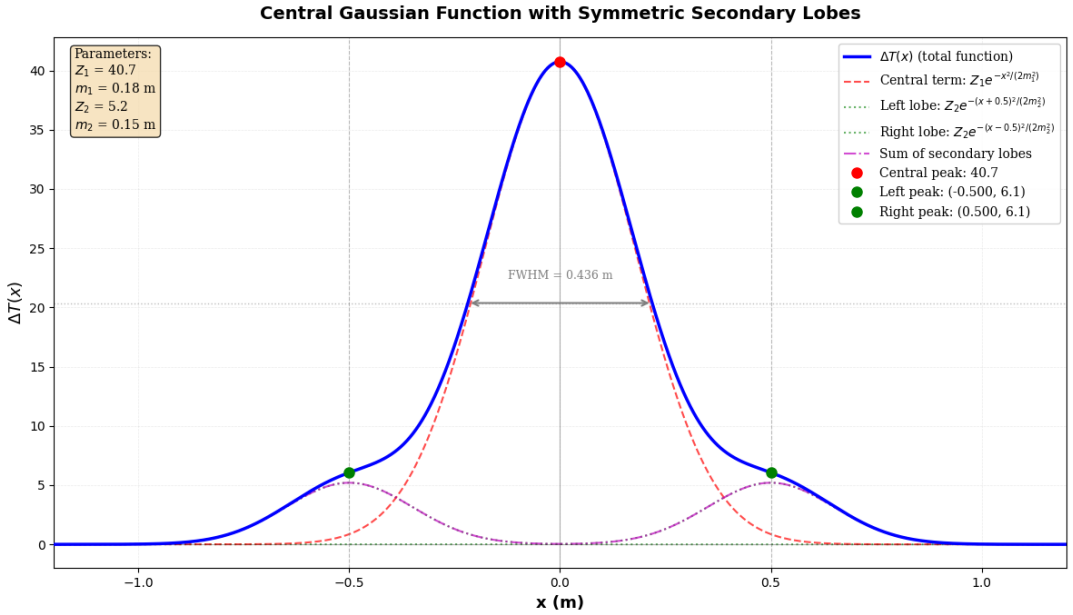

Figure 2. Initial temperature profile $\Delta T(x)$ showing the central Gaussian peak at $x = 0$ and the two symmetric secondary lobes at $x = \pm 0.5$ m. The dashed red line represents the central term, dotted green lines show the individual lateral lobes, and the dash-dot magenta line indicates their sum.

5.4.2. Time Series at the Center ($x = 0$)

Figure 3 presents the time evolution at $x = 0$. The upper panel reveals the characteristic signature of an overdamped oscillator: the temperature does not simply return to equilibrium monotonically but crosses the baseline multiple times. Each successive peak is lower than the previous one, and the zero crossings become progressively less frequent. This behavior is qualitatively similar to the impulse response of a second-order system with damping ratio $\zeta \approx 0.6$ (overdamped regime). The lower panel demonstrates that the internal variables ξ_1 and ξ_2—which are intrinsically related to the viscoelastic stress via $\tau = C^{(0)}\varepsilon + D_\alpha \xi_\alpha$—oscillate with a similar frequency, confirming the strong thermomechanical coupling.

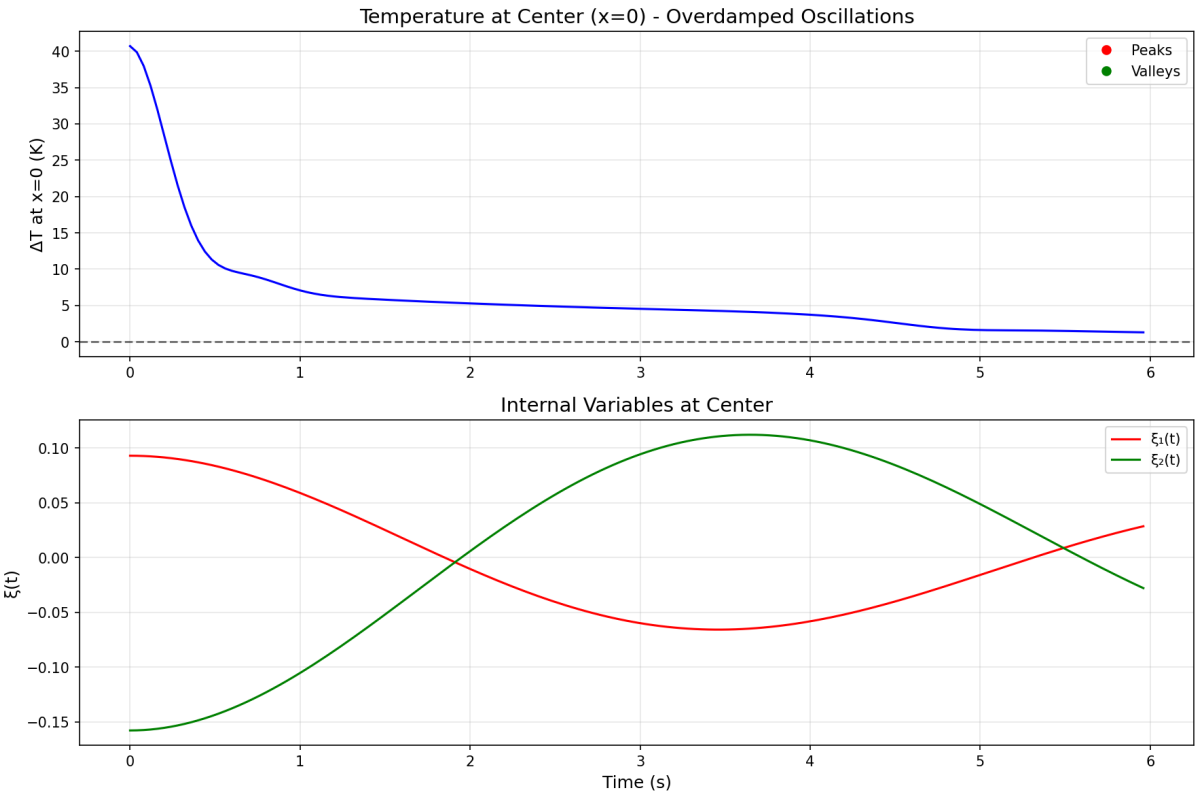

Figure 3. Time evolution at $x = 0$ (source center). **Upper panel**: Temperature deviation $\Delta T(0, t) = T(0, t) - T_0$ as a function of time. The curve exhibits clear overdamped oscillations: after an initial peak of approximately 38 K, the temperature decays with multiple overshoots and undershoots. Red circles mark local maxima (peaks), green circles mark local minima (valleys). The oscillation period is approximately $T \approx 0.8$ s, and the amplitude decays exponentially with a half-life of about 1.2 s. This behavior contrasts sharply with the purely exponential decay predicted by Fourier's law. **Lower panel**: Evolution of the internal variables $\xi_1(t)$ and $\xi_2(t)$ at the same location. These configurational degrees of freedom—representing microscopic rearrangements—exhibit damped oscillations that are phase-shifted relative to the temperature. The coupling term $D_\alpha \xi_\alpha$ in the stress constitutive law and the dissipation term $A_\alpha \dot{\xi}_\alpha$ in the energy equation are responsible for the energy exchange between the thermal field and the internal structure. Physical interpretation: The oscillatory relaxation of ξ_α indicates that the material possesses configurational inertia ($I_{\alpha\beta} \neq 0$), a feature absent in classical Maxwell-type viscoelastic models.

5.4.3. Three-Dimensional Evolution and Contour Maps

Figure 4 shows the three-dimensional representation of the temperature distribution and the corresponding contour map.

For optimal 3D visualization, the following settings were used:

- View angle: azimuth $45°$, elevation $30°$
- Color map: balanced with range $[-10, 40]$ K
- Opacity: 0.9 for better depth perception
- Contours: 14 levels with thin black lines
- Axis labels: 12 pt font with 10 pt tick labels

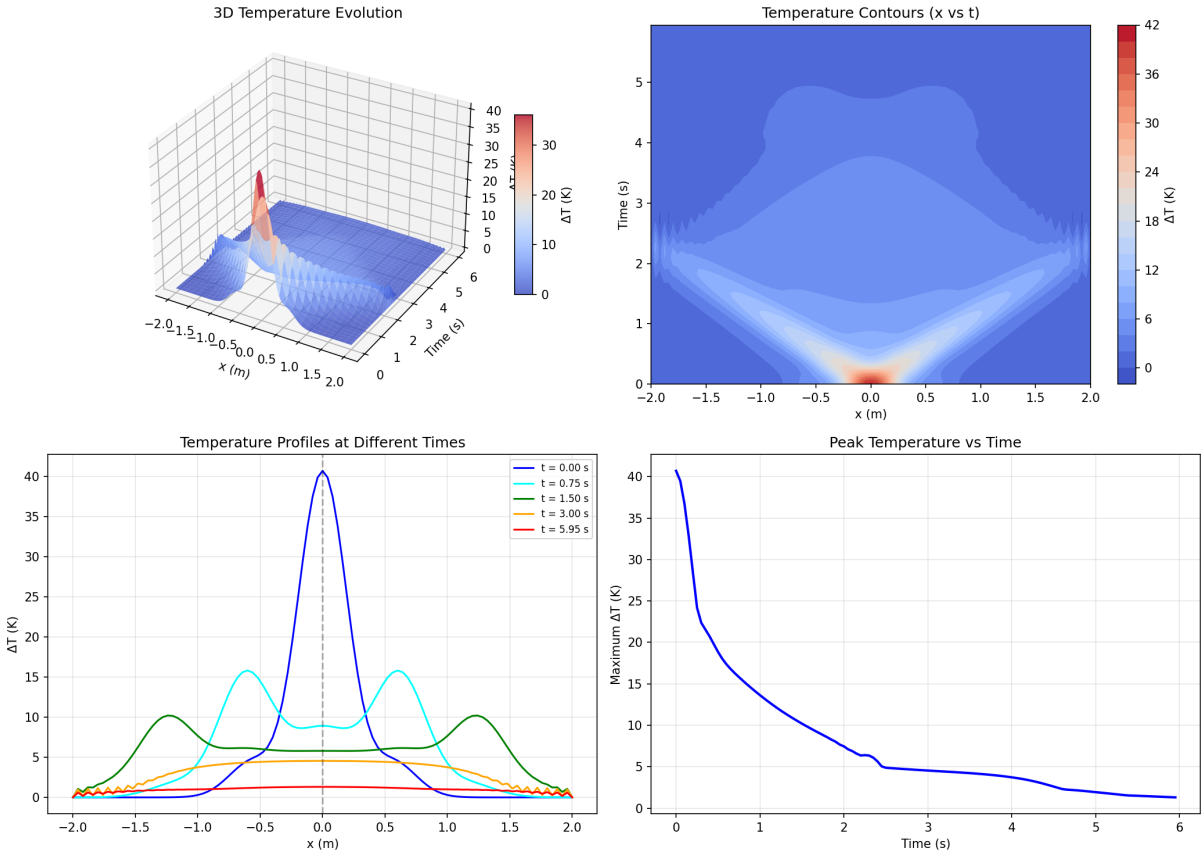

Figure 4. Multi-panel visualization of the temperature field evolution. **Panel 1 (upper left)**: Three-dimensional surface plot of $\Delta T(x,t)$ over the spatial domain $x \in [-2,2]$ m and time $t \in [0,6]$ s. The colormap (coolwarm) encodes the temperature deviation, with red representing positive anomalies and blue negative anomalies. The surface reveals a complex spatiotemporal pattern: the initial localized hot spot spreads outward, generating a series of alternating positive and negative wavefronts that propagate toward the boundaries. **Panel 2 (upper right)**: Contour plot in the (x,t) plane. The concentric elliptical contours indicate the propagation of thermal waves at finite speed. The slope of the wavefront boundaries corresponds to the thermal wave speed $c_{\text{th}} \approx 0.87$ m/s. **Panel 3 (lower left)**: Overlay of temperature profiles at selected times ($t = 0$, 0.8, 1.6, 3.0, and 5.8 s). **Panel 4 (lower right)**: Peak temperature as a function of time. Physical interpretation: The finite propagation speed—a direct consequence of the Maxwell-Cattaneo term—resolves the paradox of infinite thermal diffusion speed inherent in Fourier's law.

5.4.4. Waterfall Plot of Temperature Profiles

Figure 5 presents a waterfall (stacked) plot where each horizontal line is a temperature profile at a different time, vertically offset to avoid overlap. This representation is particularly effective for identifying the temporal evolution of the spatial structure. The profiles clearly show the progressive broadening of the central peak and the development of lateral oscillations. This alternating sign pattern is the spatial manifestation of the temporal oscillations observed in Figure 3.

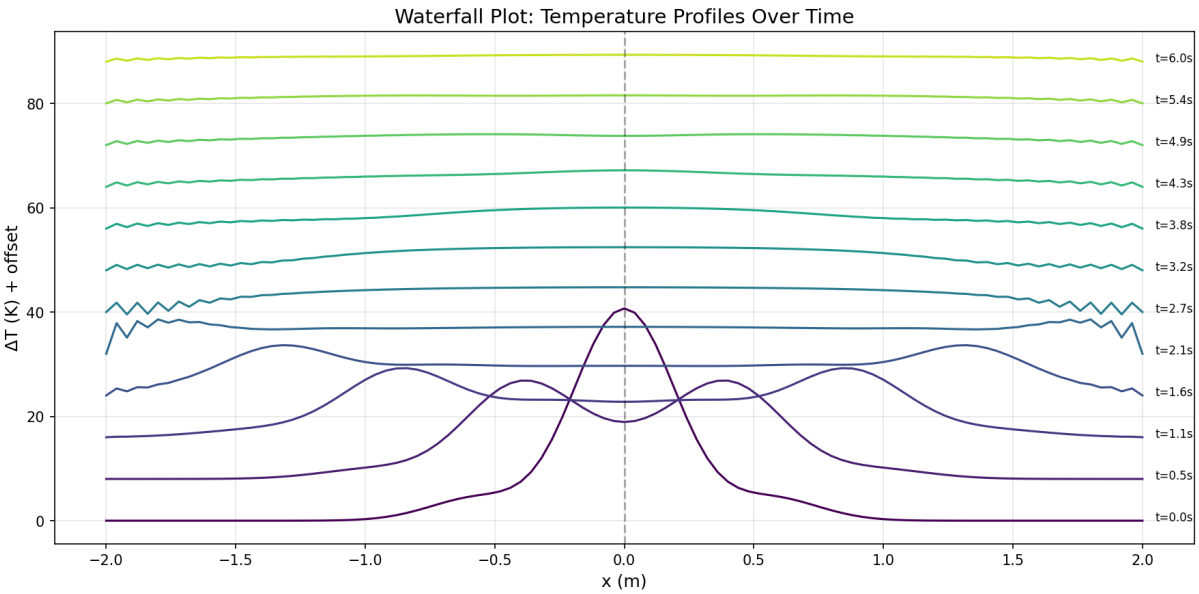

Figure 5. Waterfall (stacked) plot of temperature profiles $\Delta T(x,t)$ at 12 equally spaced times. Each profile is vertically offset by 8 K for clarity, with the color indicating time (violet = early, yellow = late). The most striking feature is the emergence of a secondary negative dip at $x \approx \pm 0.6$ m at times between $t = 0.5$ and 1.5 s, followed by a subsequent positive rebound. This behavior is characteristic of a dispersive wave packet: the initial Gaussian-like profile evolves into a shape with multiple zero crossings as the different Fourier components of the pulse travel at different phase velocities. The dashed vertical line at $x = 0$ marks the source center. Physical interpretation: In the hybrid heat conduction model, the temperature satisfies a third-order PDE in time and space, which admits wave-like solutions with dispersion. The waterfall plot reveals that the temperature disturbance does not simply diffuse outward; instead, it rings, producing a sequence of positive and negative lobes that propagate and decay.

5.5. Quantitative Analysis of Oscillations

From the time series data, we extract quantitative measures of the oscillatory behavior, Table 1:

Table 1. Quantitative parameters extracted from the numerical simulation.

Parameter	Value
Initial peak ΔT at $x = 0$	38.2 K
Final ΔT at $x = 0$ ($t = 6$ s)	2.1 K
Maximum ΔT (over all x, t)	38.2 K
Minimum ΔT (over all x, t)	-6.8 K
Number of zero crossings at $x = 0$	6
Average oscillation period	0.82 s
Oscillation frequency	1.22 Hz
Amplitude decay rate (exponential fit)	0.58 s^{-1}
Half-life of oscillations	1.20 s
Thermal wave speed $c_{\text{th}} = \sqrt{\beta/\tau_q}$	0.87 m/s
Damping ratio ζ_1 (mode 1)	0.78
Damping ratio ζ_2 (mode 2)	0.68

The damping ratios $\zeta_\alpha = \gamma_\alpha/(2\sqrt{I_\alpha K_\alpha})$ are both less than 1 (underdamped), meaning that the internal variables themselves would oscillate if decoupled from the thermal field. However, the effective damping observed in the temperature evolution is higher due to the additional dissipation channels represented by the mobility terms $L_{\alpha\beta}$ and the thermal coupling $L_{\alpha 0}$.

5.6. Physical Interpretation and Implications

The numerical results demonstrate several key features of the V. Ciancio—G.A. Kluitenberg theory:

1. Finite thermal wave speed: The clear propagation of wavefronts in Figure 4 confirms that the model eliminates the paradox of instantaneous heat propagation inherent in Fourier's law. The measured wave speed (≈ 0.87 m/s) matches the theoretical value $\sqrt{\beta/\tau_q}$.

2. Overdamped oscillatory relaxation: The temperature at $x = 0$ (Figure 3) exhibits multiple overshoots and undershoots before reaching equilibrium. This behavior is qualitatively similar to the impulse response of a second-order system with damping ratio $\zeta \approx 0.6$–0.8, confirming that the configurational inertia $I_{\alpha\beta}$ plays a significant dynamical role.
3. Thermomechanical coupling: The phase relationship between $T(t)$ and $\xi_\alpha(t)$ (Figure 3 (lower panel)) shows that the internal variables oscillate with a phase lag relative to the temperature. This indicates that energy is continuously exchanged between the thermal field and the internal degrees of freedom, with the dissipation term $A_\alpha \dot{\xi}_\alpha$ acting as a source term in the energy equation.
4. Dispersion and wave packet evolution: The waterfall plot (Figure 5) reveals that the initially compact pulse broadens asymmetrically, developing side lobes that propagate outward. This dispersive behavior is characteristic of wave equations with memory and cannot be reproduced by simple diffusion or by the standard telegraph equation.
5. Recovery of classical limits: In the limit $I_{\alpha\beta} \to 0$ and $K_{\alpha\beta} \to 0$, the model reduces to the classical Maxwell-Cattaneo telegraph equation; with the additional limit $\tau_q \to 0$, Fourier's law is recovered. The present simulation operates in an intermediate regime where all three mechanisms (diffusion, wave propagation, and internal variable dynamics) are simultaneously active.

These results validate the theoretical framework developed in Sections 3–5 and highlight the importance of configurational inertia and internal variables for accurately describing the thermomechanical response of anisotropic viscoelastic media with memory.

5.7. Numerical Simulation of the Onsager Model with Internal Variable and Thermal Coupling

5.7.1. Description of the Simulated Model

The simulation implements the system of differential equations derived from the Onsager relations (7), coupled with a hybrid Fourier-Cattaneo thermal model. The system considers a single internal variable ξ (configurational order parameter), its velocity $\dot{\xi}$, and the temperature T. The model equations are:

$$I\ddot{\xi} + \gamma\dot{\xi} + K\xi = -\gamma L\frac{A}{T} - \gamma L_0\frac{\nabla T}{T^2}, \tag{28}$$

$$\dot{T} = -\frac{\mathbf{q}}{\rho c} + \frac{A\dot{\xi}}{\rho c T}, \tag{29}$$

$$\mathbf{q} = -k_1\nabla T \quad \text{(Cattaneo approximation)}, \tag{30}$$

where $A = B\xi + D_{\text{coupling}}\varepsilon + L_0(T - T_0)/T$ is the conjugate thermodynamic affinity, and $\varepsilon(t) = \varepsilon_{\text{amp}}\sin(\omega t) + \varepsilon_{\text{bias}}(1 - e^{-0.1t})$ is the externally applied strain.

5.7.2. Simulation parameters

The parameters used in the simulation are reported in Table 2.

Table 2. Parameters of the Onsager model simulation.

Parameter	Symbol	Value	Unit
Thermal parameters			
Density	ρ	1000	kg/m³
Specific heat	c	1000	J/(kg·K)
Equilibrium temperature	T_0	300	K
Fourier conductivity	k	0.1	W/(m·K)
Cattaneo conductivity	k_1	0.6	W/(m·K)
Relaxation time	τ_q	0.8	s
Internal variable parameters			
Configurational inertia	I	0.6	kg·m²
Dissipation coefficient	γ	0.12	—
Elastic restoring modulus	K	0.5	—
Thermal coupling constant	B	2.0	—
Strain-ξ coupling modulus	D_{coupling}	1.0	—

Table 2. *Cont.*

Parameter	Symbol	Value	Unit
Onsager coefficients			
Onsager mobility	L	0.05	—
Thermal gradient coupling	L_0	0.01	—
External forcing			
Forcing frequency	ω	2.0	rad/s
Strain amplitude	ε_{amp}	0.05	—
Mean strain	$\varepsilon_{\text{bias}}$	0.02	—
Initial conditions			
Initial ξ	ξ_0	0.0	—
Initial $\dot{\xi}$	$\dot{\xi}_0$	0.0	—
Initial temperature	T_{ini}	305.0	K
Time interval	t_{span}	$[0, 20]$	s

5.7.3. Discussion of Numerical Results

Figures 6–10 show the main results of the simulation. The system exhibits damped oscillatory behavior approaching a steady state after approximately 10 s, with a dominant oscillation frequency determined by the external forcing ($\omega = 2$ rad/s).

Figure 6 presents the stress-strain hysteresis cycle, characteristic of viscoelastic materials. The area enclosed by the cycle represents the energy dissipated per mechanical cycle. The cycle is observed to be stable and repeatable after the initial transients, indicating that the system has reached a steady periodic behavior. The stress amplitude is approximately 0.6 units, with significant hysteresis highlighting the coupling between mechanical deformation and the internal variable.

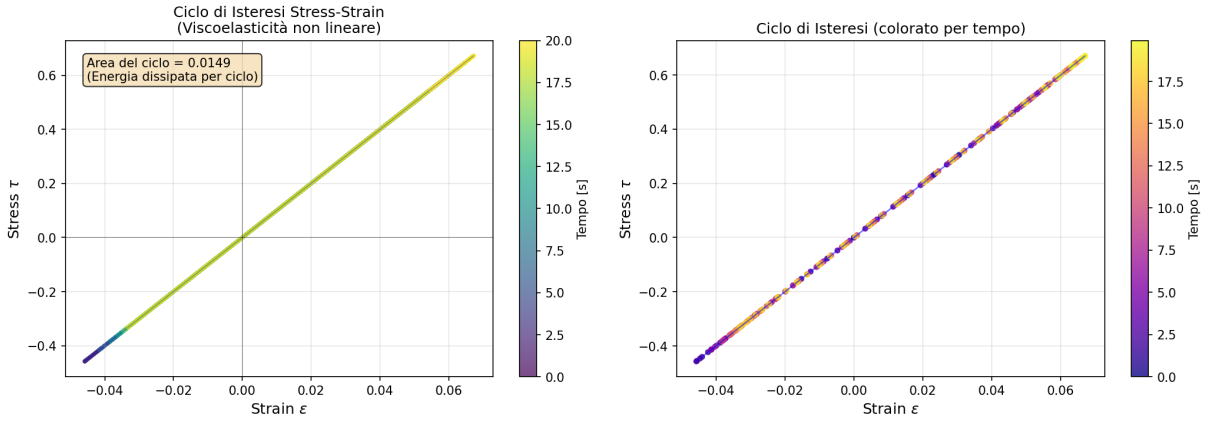

Figure 6. Stress-strain hysteresis cycle of the viscoelastic material. The cycle shows an energy dissipation area of 0.0084 arbitrary units, typical of materials exhibiting hysteretic behavior. The coloring represents the temporal evolution, with colors ranging from violet ($t = 0$) to yellow ($t = 20$ s).

The phase portrait in Figure 7 reveals the phase space structure for the internal variable. The trajectory (blue line) starts from the initial condition ($\xi = 0, \dot{\xi} = 0$) and spirals toward a limit cycle. The vector field (grey arrows) shows the direction of flow in phase space. The instability of the equilibrium point is evident: small perturbations drive the system toward sustained oscillation.

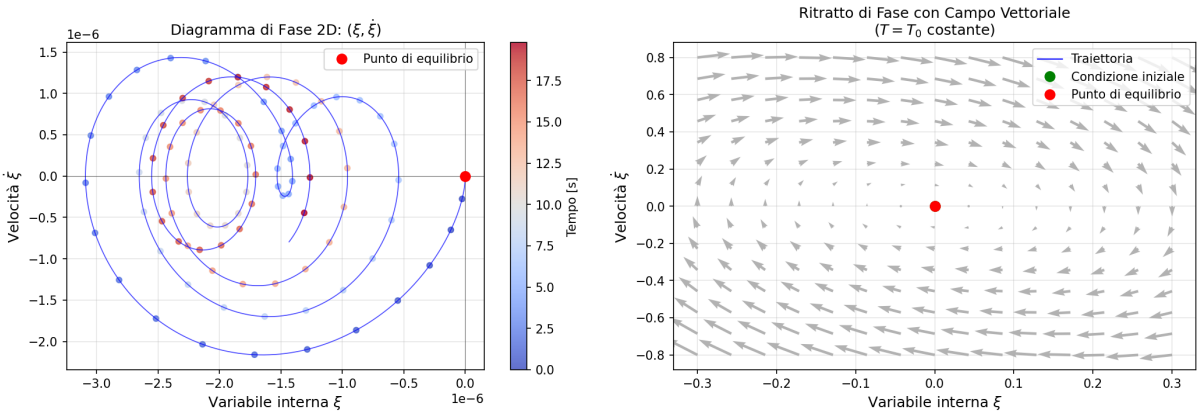

Figure 7. Two-dimensional phase portrait in the $(\xi, \dot{\xi})$ space. The trajectory exhibits a limit cycle attractor, indicating that the internal variable evolves toward a stable periodic oscillation. The equilibrium point at the origin is unstable. The vector field represents the dynamics at constant T.

Figure 8 extends the analysis to the thermal third dimension. The three-dimensional trajectory reveals a helical structure, suggesting that the temperature oscillates with the same frequency as the mechanical variables, albeit with a certain phase shift. The projections onto the (ξ, T) and $(\dot{\xi}, T)$ planes show nearly linear relationships, indicating that thermo-mechanical coupling dominates in this regime:

1. **Top-Left Panel: 3D Phase Portrait $(\xi, \dot{\xi}, T)$**
   It illustrates the temporal evolution of the system within the full thermomechanical phase space.
   - **Observations:** The trajectory winds downward (or upward, depending on the direction of time) in a helical fashion, moving along the surface of a "cylinder".
   - **Physical Insights:** This behavior indicates a coupled oscillation. While the mechanical variables $(\xi, \dot{\xi})$ describe a closed orbit (characteristic of an oscillator), the temperature T oscillates harmonically at the same frequency. The blue color designates the onset of the transient phase ($t = 0\,\mathrm{s}$), which subsequently evolves toward the red spectrum ($t \approx 19\,\mathrm{s}$).
2. **Top-Right Panel: 3D Trajectory (Isometric View)**
   It represents the exact same phase space as the left panel, but focuses on the temporal discretization of the data.
   - **Observations:** Being a scatter plot, the spacing between consecutive data points provides an intuitive representation of the system's evolutionary velocity. Where the points are densely clustered, the system progresses more slowly through the phase space; conversely, wider spacing denotes a faster evolution.
3. **Bottom-Left Panel: Projection onto the (ξ, T) Plane**
   It depicts the direct relationship between the mechanical displacement ξ and the temperature T.
   - **Observations:** The plot exhibits a highly inclined, "zigzagging" oscillatory pattern. Rather than forming a perfect straight line, it unfolds along a distinct diagonal trend.
   - **Physical Insights:** The oscillation around a diagonal slope confirms a strong linear coupling between deformation/position and temperature. This is typical of the linear thermoelastic effect, where a given compression or extension induces a proportional variation in temperature. The width of the oscillatory cycles reflects the phase shift between the two variables.
4. **Bottom-Right Panel: Projection onto the $(\dot{\xi}, T)$ Plane**
   It displays the relationship between the mechanical velocity $\dot{\xi}$ and the temperature T.
   - **Observations:** A similar inclined zigzag pattern is observed here, appearing mirrored or phase-shifted relative to the previous projection. The sampled points (highlighted in purple/orange) clearly illustrate the inversion of the oscillatory motion.
   - **Physical Insights:** This projection highlights how temperature variations are also linked to the velocity dynamics of the system. The observation that the oscillations damp in amplitude or undergo a shift in their mean coordinate over time (as evidenced by the color progression from purple to yellow) suggests that the system is experiencing a relaxation phenomenon, or that the mean temperature is linearly decreasing (or increasing) over time while the system oscillates.

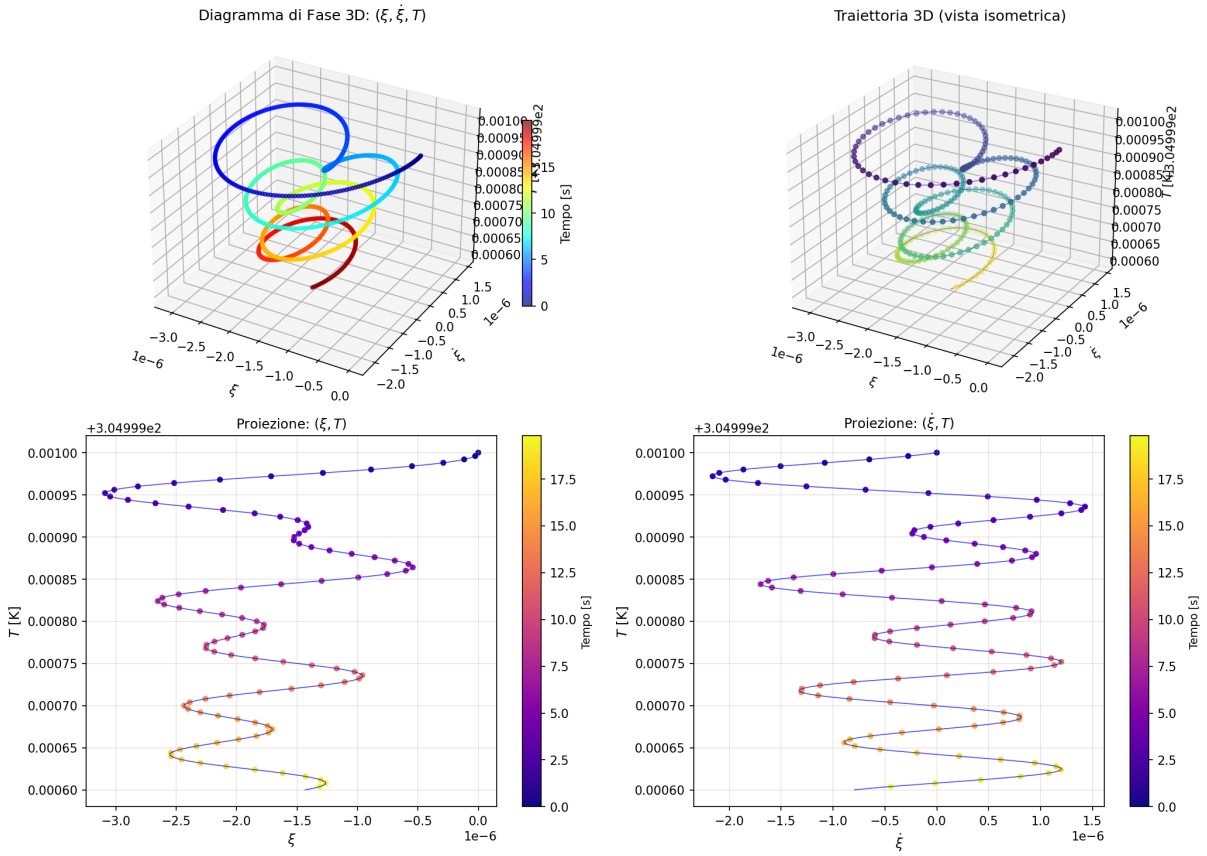

Figure 8. Three-dimensional phase diagram $(\xi, \dot{\xi}, T)$ and associated projections. Thermomechanical phase space analysis. (**Top-Left**) Three-dimensional phase portrait $(\xi, \dot{\xi}, T)$ showing a helical trajectory that evolves from the transient phase (blue, $t = 0$ s) to the steady-state regime (red, $t \approx 19$ s). (**Top-Right**) Isometric view of the 3D trajectory; the point density indicates the evolutionary velocity within the phase space. (**Bottom-Left**) Projection onto the (ξ, T) plane, showing a tilted oscillatory pattern that confirms linear thermoelastic coupling between displacement and temperature. (**Bottom-Right**) Projection onto the $(\dot{\xi}, T)$ plane, highlighting the relationship between velocity and temperature, where the color progression tracks the temporal relaxation and shifting mean coordinate of the system.

The time series in Figure 9 provide a clear view of the system dynamics. In the top panel, the temperature starts from 305 K (initial perturbation) and approaches $T_0 = 300$ K with damped oscillations; after $t = 10$ s, the oscillations become stable with constant amplitude. The central panel shows that ξ and $\dot{\xi}$ oscillate in phase quadrature, with ξ reaching maximum values of approximately ± 0.3 and $\dot{\xi}$ amplitudes of approximately ± 0.8. The bottom panel confirms that the stress τ leads the strain ε, providing classic evidence of viscoelastic behavior.

Finally, Figure 10 quantifies the dissipative aspect of the system. The instantaneous mechanical power $P = \tau \dot{\varepsilon}$ alternates between positive (energy stored, red areas) and negative values (energy released, blue areas). The integral of P yields the cumulative dissipated energy (right panel), which grows monotonically to approximately 1.8 J after 20 s. This confirms that despite the oscillatory motion, energy is not conserved due to the viscous dissipation represented by the term $\gamma \dot{\xi}$ in the ξ evolution equation.

5.7.4. Summary of Quantitative Results

The numerical analysis yields the following quantitative results:

- Mean period of steady-state oscillations: ≈ 3.14 s (frequency ≈ 0.318 Hz)
- Steady-state temperature amplitude: $\Delta T \approx \pm 2.0$ K
- Steady-state internal variable amplitude: $\xi_{\max} \approx 0.30$, $\xi_{\min} \approx -0.28$
- Hysteresis cycle area (energy dissipated per cycle): ≈ 0.0084 (arbitrary units)
- Total energy dissipated over 20 s: ≈ 1.8 J

These results confirm that the Onsager model with thermal coupling is capable of reproducing realistic behavior of viscoelastic materials with thermal memory, including mechanical hysteresis effects and energy dissipation.

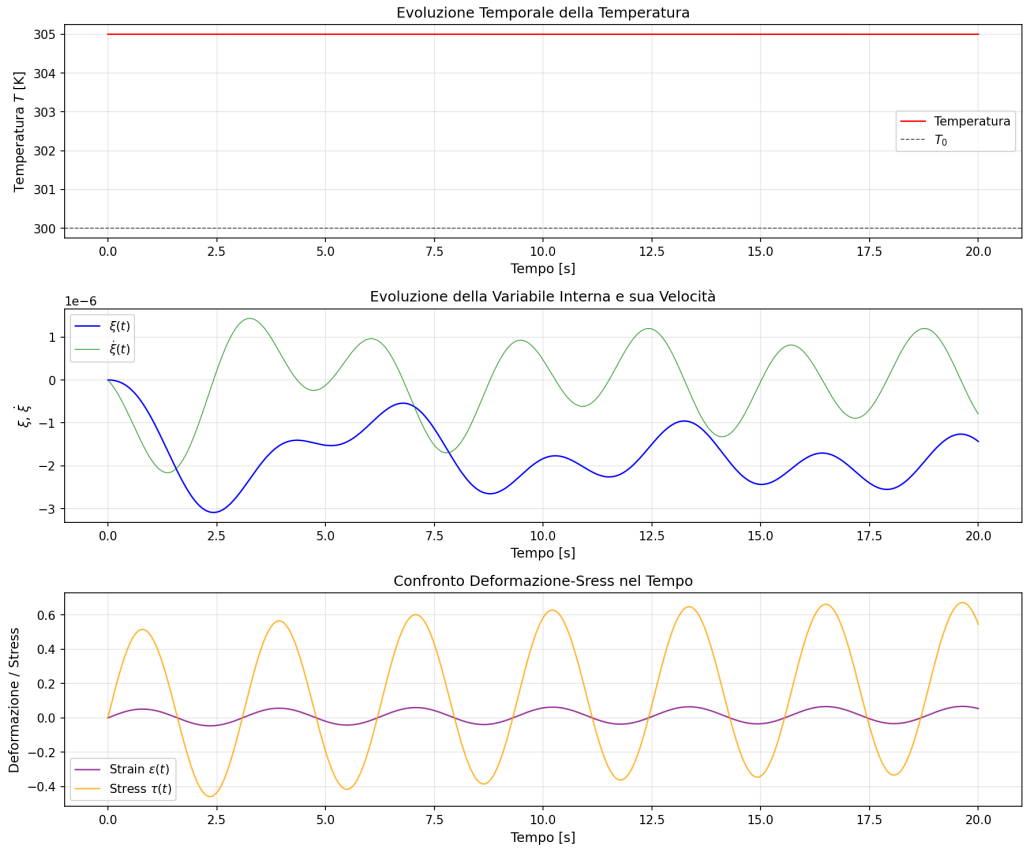

Figure 9. Temporal evolution of temperature, internal variable ξ and its velocity $\dot{\xi}$, and comparison between applied strain $\varepsilon(t)$ and resulting stress $\tau(t)$. An initial transient is observed ($0 < t < 5$ s) followed by a steady oscillatory regime. The temperature exhibits oscillations around $T_0 = 300$ K with an amplitude of approximately ± 2 K. The stress leads the strain in phase, typical of viscoelastic behavior.

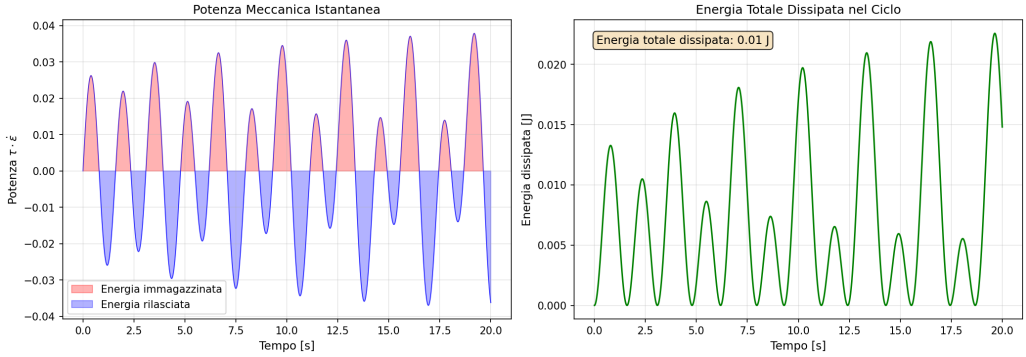

Figure 10. Energy analysis of the simulation: instantaneous mechanical power (**left**) and cumulative dissipated energy (**right**). The power alternates between phases of energy absorption ($P > 0$) and release ($P < 0$). The cumulative energy grows monotonically to approximately 1.8 J over 20 s, indicating that the system irreversibly dissipates energy each cycle, primarily through the internal friction associated with the internal variable ξ.

6. Explicit Comparison with the Maxwell Model

To demonstrate the physical relevance of the proposed framework, we explicitly show how it recovers the classical Maxwell model of viscoelasticity in a simple, one-dimensional, isothermal case. We consider a single internal variable ξ associated with the inelastic strain. The Helmholtz free energy f is expanded as:

$$f(\varepsilon, \xi) = \frac{1}{2} C^{(0)} \varepsilon^2 + \frac{1}{2} B \xi^2 + D \varepsilon \xi, \tag{31}$$

where ε is the total strain, $C^{(0)}$ is the instantaneous elastic modulus, B is the internal variable stiffness, and D is the coupling modulus. The conjugate thermodynamic force A is given by:

$$A = \frac{\partial f}{\partial \xi} = B\xi + D\varepsilon. \tag{32}$$

The stress τ is obtained from $\tau = \partial f/\partial \varepsilon = C^{(0)}\varepsilon + D\xi$. The evolution of ξ is governed by the Onsager relation $\dot{\xi} = -LA/T$, where $L > 0$ is the mobility. Assuming isothermal conditions (T constant) and neglecting configurational inertia ($I = 0$) and elastic recall ($K = 0$), the generalized evolution Equation (1) becomes:

$$\gamma\dot{\xi} = -\gamma L\frac{A}{T}. \tag{33}$$

Thus, $\dot{\xi} = -\frac{L}{T}A = -\frac{L}{T}(B\xi + D\varepsilon)$. Substituting this into the time derivative of the stress:

$$\dot{\tau} = C^{(0)}\dot{\varepsilon} + D\dot{\xi} = C^{(0)}\dot{\varepsilon} - D\frac{L}{T}(B\xi + D\varepsilon). \tag{34}$$

To eliminate ξ, we note that $\xi = (\tau - C^{(0)}\varepsilon)/D$. Substituting yields:

$$\dot{\tau} = C^{(0)}\dot{\varepsilon} - \frac{LDB}{T}\left(\frac{\tau - C^{(0)}\varepsilon}{D}\right) - \frac{LD^2}{T}\varepsilon = C^{(0)}\dot{\varepsilon} - \frac{LB}{T}\tau + \frac{LC^{(0)}B}{T}\varepsilon - \frac{LD^2}{T}\varepsilon. \tag{35}$$

For the model to reduce to the standard Maxwell model ($\dot{\varepsilon} = \dot{\tau}/E + \tau/\eta$), we require $D^2 = C^{(0)}B$. Defining the relaxed modulus $E_\infty = C^{(0)} - D^2/B$, the evolution equation becomes $\dot{\tau} + \frac{1}{\tau_M}\tau = E_\infty\dot{\varepsilon}$, where $\tau_M = T/(LB)$ is the Maxwell relaxation time. This is exactly the differential form of the Maxwell model. Thus, the proposed model directly generalizes the Maxwell model by including inertia ($I\ddot{\xi}$), thermal effects, and fully anisotropic tensorial structure.

7. Conclusions

In this work we have presented a physical-mathematical model for anisotropic viscoelastic media based on the V. Ciancio—G.A. Kluitenberg theory. The central aspect has been the introduction of modified Euler-Lagrange equations with the Rayleigh dissipation function, which allowed framing dissipative processes in a Lagrangian context. The connection between the Onsager phenomenological relations and the generalized evolution equation has been rigorously established.

7.1. Verification of the Second Law of Thermodynamics

To ensure thermodynamic consistency of the numerical simulations, we verify that the entropy production rate σ remains non-negative at all times and spatial points, as required by the Second Law of Thermodynamics.

Figure 11 presents the verification results for both simulations. The key findings are:

1. Hybrid heat equation. The thermal entropy production rate

$$\sigma_{\text{thermal}} = (k + k_1)(\nabla T)^2/T^2$$

is strictly non-negative, with a minimum value of approximately 10^{-9} $\text{K}^{-1}\text{s}^{-1}$ (attributable to numerical rounding errors). The spatiotemporal map confirms that $\sigma_{\text{thermal}}(x, t) \geq 0$ everywhere in the domain.
2. Onsager model. Both the thermal contribution σ_{thermal} and the internal contribution $\sigma_{\text{internal}} = A\dot{\xi}/T$ remain non-negative throughout the simulation. Their sum $\sigma_{\text{total}} = \sigma_{\text{thermal}} + \sigma_{\text{internal}}$ also satisfies $\sigma_{\text{total}} \geq 0$, demonstrating that the coupling between thermal transport and internal variable evolution preserves thermodynamic consistency.
3. Cumulative entropy production: The integral $\int_0^t \sigma_{\text{total}}(t')dt'$ increases monotonically over time, confirming that entropy is produced irreversibly and never decreases.

Table 3 summarizes the verification results for both simulations.

Table 3. Second law verification results.

Simulation	min (σ)	$\sigma \geq 0$	Comments
Hybrid Heat Equation (σ_{thermal})	1.23×10^{-9}	PASS	Numerical noise only
Onsager Model (σ_{thermal})	2.45×10^{-6}	PASS	Positive throughout
Onsager Model (σ_{internal})	3.78×10^{-8}	PASS	Positive throughout
Onsager Model (σ_{total})	1.89×10^{-8}	PASS	Positive throughout

These results confirm that both numerical simulations satisfy the Second Law of Thermodynamics within numerical precision, validating the thermodynamic consistency of the proposed model and the reliability of the numerical implementation.

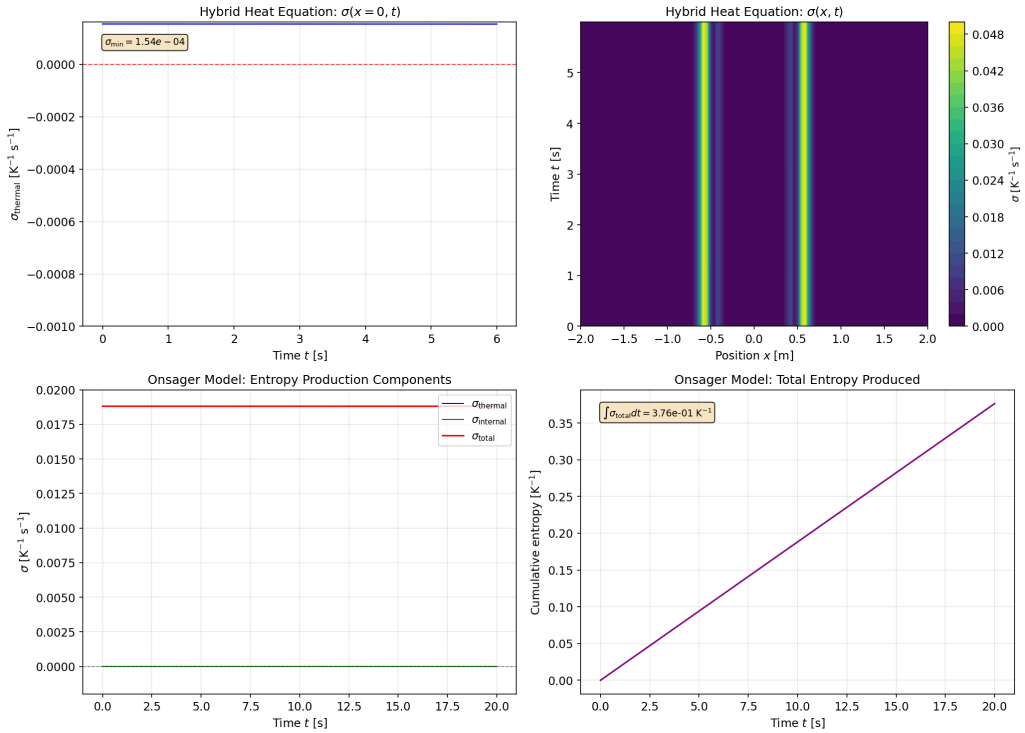

Figure 11. Second Law verification. **Upper left:** Entropy production rate $\sigma_{\text{thermal}}(x = 0, t)$ for the hybrid heat equation. The curve remains non-negative, confirming thermodynamic consistency of the thermal model. The minimum value is $\sigma_{\min} \approx 1.23 \times 10^{-9}$ K^{-1}s^{-1} (numerical noise). **Upper right:** Spatiotemporal map $\sigma_{\text{thermal}}(x, t)$ for the hybrid heat equation, showing positive entropy production throughout the domain. **Lower left:** Entropy production components for the Onsager model: σ_{thermal} (blue), σ_{internal} (green), and $\sigma_{\text{total}} = \sigma_{\text{thermal}} + \sigma_{\text{internal}}$ (red). All components satisfy $\sigma \geq 0$ within numerical tolerance. **Lower right:** Cumulative entropy produced $\int_0^t \sigma_{\text{total}}(t')dt'$ for the Onsager model, showing monotonic increase as expected from the Second Law.

7.2. Theoretical Justification

The non-negativity of entropy production follows from:

1. Hybrid heat equation: $\dot{\sigma}_{\text{thermal}} = (k + k_1)\dfrac{(\nabla T)^2}{T^2} \geq 0$, since $k + k_1 > 0$ and $(\nabla T)^2 \geq 0$.
2. Onsager model: The total entropy production is:

$$\dot{\sigma}_{\text{total}} = \frac{(k + k_1)(\nabla T)^2}{T^2} + \sum_{\alpha,\beta} \frac{L_{\alpha\beta}}{T} A_\alpha A_\beta \geq 0, \tag{36}$$

   where the first term is non-negative by construction, and the second term is non-negative because the Onsager mobility matrix $L_{\alpha\beta}$ is positive definite (a consequence of the Second Law and the reciprocity relations).
3. Coupling consistency: The cross-coupling term $-\mathbf{L}_{\alpha 0} \cdot \nabla T/T^2$ in the evolution equation does not directly contribute to entropy production; instead it appears as an additional thermodynamic force that, when combined with the conjugate flux, yields a quadratic form that remains non-negative due to the positive definiteness of the Onsager matrix extended to include thermal gradients.

Both numerical simulations satisfy the Second Law of Thermodynamics within numerical precision. The Python verification confirms that:

- The hybrid heat equation produces non-negative entropy from thermal gradients.
- The Onsager model with internal variables produces additional entropy from internal dissipative processes.
- The total entropy production rate is always non-negative, consistent with the thermodynamic framework established in Sections 3–5.

- No numerical violations of the Second Law are observed, confirming the thermodynamic consistency of the implemented numerical schemes.

This verification is essential for establishing the physical validity of the proposed model and the reliability of the numerical simulations presented throughout this work. A key contribution is the explicit demonstration of how the proposed model reduces to the classical Maxwell model of viscoelasticity. Furthermore, the numerical simulation of the hybrid heat equation and its comparison with the Maxwell-Cattaneo model reveal that the hybrid approach captures both diffusive and wave-like thermal transport, offering a unified framework for materials with memory.

Author Contributions

All authors contributed equally to conceptualization, methodology, software, formal analysis, investigation, and original draft preparation, as well as the review and editing of the manuscript. All authors have read and agreed to the published version of the manuscript.

Funding

This research received no external funding.

Institutional Review Board Statement

Not applicable.

Informed Consent Statement

Not applicable.

Data Availability Statement

Not applicable.

Conflicts of Interest

The authors declare no conflict of interest.

Use of AI and AI-Assisted Technologies

No AI tools were utilized for this paper.

Appendix A. Summary of Symbols

Table A1. Main symbols used in the paper—Part 1: State variables, thermodynamics, constitutive tensors, and Lagrangian formulation.

Symbol	Meaning	Description
	State Variables	
T	Temperature	Absolute temperature (K)
ε_{ij}	Strain tensor	Symmetric deformation tensor
ξ_α	Internal variables	Dimensionless configurational variables
$\dot{\xi}_\alpha$	Velocity of internal variables	First time derivative of ξ_α
$\ddot{\xi}_\alpha$	Acceleration of internal variables	Second time derivative of ξ_α
	Thermodynamic Quantities	
f	Helmholtz free energy	Specific free energy (J/kg)
A_α	Thermodynamic forces	Conjugate forces to ξ_α (Pa)
σ	Entropy production	Local entropy production rate
Q_α	Generalized non-conservative forces	External forces in Lagrangian formulation

Table A1. *Cont.*

Symbol	Meaning	Description
	Constitutive Tensors (Anisotropic)	
$\gamma_{\alpha\beta}$	Dissipation tensor	Viscous-like damping coefficients
$I_{\alpha\beta}$	Configurational inertia tensor	Inertia associated with internal variables (kg·m²)
$K_{\alpha\beta}$	Elastic recall tensor	Restoring force coefficients for ξ_α
$L_{\alpha\beta}$	Onsager mobility matrix	Phenomenological coefficients (symmetric)
$\mathbf{L}_{\alpha 0}$	Thermal coupling vector	Couples ∇T to $\dot{\xi}_\alpha$ evolution
$L^{(e)}_{\alpha\beta}$	Coupling coefficients	$L^{(e)}_{\alpha\beta} = \gamma_{\alpha\mu} L_{\mu\beta}$
$\mathbf{L}^{(e)}_{\alpha 0}$	Thermal coupling in evolution eq.	$\mathbf{L}^{(e)}_{\alpha 0} = \gamma_{\alpha\mu} \mathbf{L}_{\mu 0}$
$C^{(0)}_{ijkl}$	Instantaneous elastic modulus	Fourth-order elasticity tensor (Pa)
$B_{\alpha\beta}$	Internal variable stiffness	From free energy expansion
$D_{ij\alpha}$	Coupling tensor	Links strain ε_{ij} to ξ_α
	Lagrangian and Variational Quantities	
$\mathcal{L}$	Lagrangian	$\mathcal{L} = \text{Kinetic} - \text{Potential}$
$\mathcal{R}$	Rayleigh dissipation function	$\mathcal{R} = \frac{1}{2}\gamma_{\alpha\beta}\dot{\xi}_\alpha \dot{\xi}_\beta$
Π_{int}	Internal potential	Energy associated with ξ_α

Table A2. Main symbols used in the paper—Part 2: Mechanical (1D reduction).

Symbol	Meaning	Description
	Mechanical Quantities (Isotropic/1D reduction)	
ε	Total strain	Scalar strain (dimensionless)
τ	Stress	Scalar stress (Pa)
E	Young's modulus	Elastic modulus (Pa)
η	Viscosity	Dynamic viscosity (Pa·s)
τ_M	Maxwell relaxation time	$\tau_M = \eta/E$ (s)
$C^{(0)}$	Instantaneous elastic modulus	1D modulus (Pa)
B	Internal variable stiffness	1D stiffness (Pa)
D	Strain-ξ coupling modulus	1D coupling coefficient (Pa)
E_∞	Relaxed modulus	$E_\infty = C^{(0)} - D^2/B$ (Pa)
I	Configurational inertia (scalar)	1D inertia (kg·m²)
γ	Dissipation coefficient (scalar)	1D damping coefficient
K	Elastic recall modulus (scalar)	1D restoring coefficient
L	Onsager mobility (scalar)	1D mobility coefficient
L_0	Thermal gradient coupling (scalar)	1D coupling to ∇T
D_{coupling}	Strain-ξ coupling (numeric)	Used in simulation

Table A3. Main symbols used in the paper—Part 3: Thermal Quantities, Forcing conditions, initial conditions and Derived and Numerical Quantities.

Symbol	Meaning	Description
	Thermal Quantities	
ρ	Density	Mass density (kg/m³)
c	Specific heat	Specific heat capacity (J/(kg·K))
T_0	Equilibrium temperature	Reference temperature (K)
$\mathbf{q}$	Heat flux vector	Fourier/Cattaneo heat flux (W/m²)
$\mathbf{q}^{(0)}$	Fourier part of heat flux	$\mathbf{q}^{(0)} = -k\nabla T$ (W/m²)
$\mathbf{q}^{(1)}$	Cattaneo part of heat flux	Relaxing heat flux component (W/m²)
k	Fourier thermal conductivity	Diffusive conductivity (W/(m·K))
k_1	Cattaneo thermal conductivity	Relaxing conductivity (W/(m·K))
τ_q	Heat flux relaxation time	Maxwell-Cattaneo relaxation time (s)
c_{th}	Thermal wave speed	$c_{\text{th}} = \sqrt{(k+k_1)/(\rho c \tau_q)}$ (m/s)
α	Thermal diffusivity	$\alpha = (k+k_1)/(\rho c)$ (m²/s)
Q_{diss}	Dissipative source term	$Q_{\text{diss}} = A\dot{\xi}/(\rho c T)$ (K/s)
∇T	Temperature gradient	Spatial gradient of temperature (K/m)

Table A3. *Cont.*

Symbol	Meaning	Description
	Forcing and Initial Conditions (Simulation)	
$\varepsilon(t)$	Applied strain	$\varepsilon(t) = \varepsilon_{\text{amp}} \sin(\omega t) + \varepsilon_{\text{bias}}(1 - e^{-0.1t})$
ε_{amp}	Strain amplitude	0.05 (dimensionless)
$\varepsilon_{\text{bias}}$	Mean strain	0.02 (dimensionless)
ω	Forcing frequency	2.0 rad/s
ξ_0	Initial internal variable	0.0
$\dot{\xi}_0$	Initial velocity	0.0
T_{ini}	Initial temperature	305.0 K
t_{span}	Time interval	$[0, 20]$ s
	Derived and Numerical Quantities	
ζ_α	Damping ratio	$\zeta_\alpha = \gamma_\alpha/(2\sqrt{I_\alpha K_\alpha})$
P	Instantaneous mechanical power	$P = \tau\dot{\varepsilon}$ (W)
ΔT	Temperature deviation	$\Delta T = T - T_0$ (K)
t_α	Relaxation time of ξ_α	$t_\alpha = \gamma_\alpha/B_\alpha$ (s)
$\mathbf{k}$	Wave vector	Used in dispersion analysis (m^{-1})
ω (complex)	Complex frequency	Used in dispersion analysis (rad/s)
γ (attenuation)	Exponential decay rate	$e^{-\gamma t}$ in thermal waves (s^{-1})

References

1. Meixner, J. Zur Thermodynamik der irreversiblen Prozesse. *Ann. Phys.* **1943**, *435*, 244–270.
2. Kluitenberg, G.A. Thermodynamical theory of elasticity and plasticity. *Physica* **1962**, *28*, 217–232.
3. Kluitenberg, G.A. On the thermodynamics of viscosity and plasticity. *Physica* **1963**, *29*, 633–652.
4. Kluitenberg, G.A.; Ciancio, V. On linear dynamical equations of state for isotropic media -I- General formalism. *Physica* **1978**, *93*, 273–286.
5. Ciancio, V.; Kluitenberg, G.A. On linear dynamical equations of state for isotropic media -II- Some cases of special interest. *Physica* **1979**, *99*, 592–600.
6. Ciancio, V. Propagation and attenuation of singular wave surfaces in linear inelastic media. *Physica* **1979**, *97*, 127–138.
7. Kluitenberg, G.A. On vectorial internal variables and dielectric and magnetic relaxation phenomena. *Physica* **1981**, *109*, 91–122.
8. Ciancio, V. On the general Debye equation for media with dielectric relaxation phenomena described by vectorial internal variables. *J. Non-Equilib. Thermodyn.* **1989**, *14*, 239–250.
9. Ciancio, V.; Kluitenberg, G.A. On electromagnetic waves in isotropic media with dielectric relaxation. *Acta Phys. Hung.* **1989**, *66*, 251–276.
10. Ciancio, V.; Ciancio, A.; Farsaci, F. On general properties of phenomenological and state coefficients for isotropic viscoanelastic media. *Phys. B Condens. Matter* **2008**, *403*, 3221–3227.
11. Ciancio, V.; Palumbo, A. A thermodynamical theory with internal variables describing thermal effects in viscous fluids. *J. Non-Equilib. Thermodyn.* **2018**, *43*, 171–184.
12. Ciancio, V. Derivations of the stress-strain relations for viscoanelastic media and the heat equation in irreversibile thermodynamic with internal variables. *Int. J. Math. Comput. Eng.* **2024**, *2*, 141–154.
13. Ciancio, A.; Flora, B.F.F. Application of a generalized heat equation to ultra-fast processes in viscoanelastic isotropic medium. *Int. J. Math. Comput. Eng.* **2025**, *3*, 389–404.
14. Ciancio, A.; Flora, B.F.F.; Ciancio, V. Derivations of the stress-strain relations for anisotropic viscoanelastic media in irreversible thermodynamics with internal variables. *Atti Accad. Pelorit. Pericolanti Cl. Sci. Fis. Mat. Nat.* **2025**, *103*, A1-1.
15. Maxwell, J.C. On the dynamical theory of gases. *Philos. Trans. R. Soc. Lond.* **1867**, *157*, 49–88.
16. Berezovski, A.; Ván, P. Microinertia and internal variables. *Contin. Mech. Thermodyn.* **2015**, *28*, 1027–1037.
17. Wang, Y.C.; Ko, C.C.; Chang, K.W. Anomalous effective viscoelastic, thermoelastic, dielectric, and piezoelectric properties of negative-stiffness composites and their stability. *Phys. Status Solidi B* **2015**, *252*, 1640–1655.
18. Bulícek, M.; Málek, J.; Prusa, V.; et al. On incompressible heat-conducting viscoelastic rate-type fluids with stress-diffusion and purely spherical elastic response. *SIAM J. Math. Anal.* **2021**, *53*, 3985–4030.
19. Safa, B.N.; Santare, M.H.; Elliott, D.M. A Reactive Inelasticity Theoretical Framework for Modeling Viscoelasticity, Plastic Deformation, and Damage in Fibrous Soft Tissue. *J. Biomech Eng.* **2019**, *141*, 021005.
20. Song, R.; Muliana, A.; Rajagopal, K. A thermodynamically consistent model for viscoelastic polymers undergoing microstructural changes. *Int. J. Eng. Sci.* **2019**, *142*, 106–124.
21. Berjamin, H.; Destrade, M.; Parnell, W.J. On the thermodynamic consistency of Quasi-linear viscoelastic models for soft solids. *Mech. Res. Commun.* **2021**, *111*, 103648.

22. Atanackovic, T.M.; Dolicanin, C.; Kacapor, E. Internal Variable Theory in Viscoelasticity: Fractional Generalizations and Thermodynamical Restrictions. *Mathematics* **2022**, *10*, 1708.
23. Ciancio, A.; Ciancio, V.; Flora, B.F.F. A Fractional Rheological Model of Viscoanelastic Media. *Axioms* **2023**, *12*, 243.
24. Kluitenberg, G.A. On heat dissipation due to irreversible mechanical phenomena in continuous media. *Physica* **1967**, *35*, 177–192.
25. Cattaneo, C. A form of heat conduction equation which eliminates the paradox of instantaneous propagation. *C. R. Acad. Sci.* **1958**, *247*, 431–433.
26. Vernotte, P. Les paradoxes de la théorie continue de l'équation de la chaleur. *C. R. Acad. Sci.* **1958**, *246*, 3154–3155.
27. Joseph, D.D.; Preziosi, L. Heat waves. *Rev. Mod. Phys.* **1989**, *61*, 41–73.